Int. J. Electrochem. Sci., 16 **(2021)** Article ID: 210461, doi: 10.20964/2021.04.20

International Journal of
ELECTROCHEMICAL
SCIENCE
www.electrochemsci.org

Short Communication

One pot synthesis of Fe_2O_3-reduced graphene nanocomposite as cathode material for Lithium Ion Batteries

Shuiqin Zhou, Wenbin Pan, Chu Chen, Lepeng Lin, Weigang Guo[*]

Fair Friend Institute of Intelligent Manufacturing, Hangzhou Vocational and Technical College, 310018, P.R. China
[*]E-mail: guoweigang@vtcuni.com

Received: 28 November 2020 / *Accepted:* 18 January 2021 / *Published:* 28 February 2021

Due to their advantages of a high voltage, high specific capacity, long cycling life, low pollution, etc., lithium-ion batteries are widely used in consumer electronics, such as smart phones and laptops. Fe_2O_3 is chosen as the object of study in this work. Combining Fe_2O_3 with RGO allows for combining the advantages of a high specific surface area, high stability and high electrical conductivity to produce a new material for high-performance cathodes. The Fe_2O_3/RGO composite exhibits a remarkably high reversible specific capacity of 1582 mAh/g with a specific discharge capacity of 812 mAh/g at 0.1C after 100 cycles.

Keywords: Lithium-ion batteries; Cathode materials; Graphene; Fe_2O_3; Hydrothermal

1. INTRODUCTION

At present, lead-acid batteries, nickel cadmium batteries, nickel hydrogen batteries and lithium-ion batteries are the most common chemical power supplies. Among them, lead-acid batteries are the widely used traditional battery. Although they have established manufacturing technology and are inexpensive, their energy density is low, and they easily cause serious environmental pollution during production and use. With the development of society and the large increase in environmental protection awareness, it is imperative to vigorously develop new, efficient, and environmentally friendly batteries [1–7]. As a kind of green secondary power supply, lithium-ion batteries have the advantages of a high working voltage, large specific capacity, long cycling life and no production of pollution; thus, lithium-ion batteries are widely used in smart phones, notebook computers and other consumer electronic products. Furthermore, the high specific energy of lithium-ion batteries as a portable power supply and power battery show attractive prospects; thus, they have become a focus of attention worldwide and have been widely studied by many researchers.

Graphene, as a new type of nanocarbon material, has shown excellent physical and chemical properties, such as an ultrahigh specific surface area, good electrical and thermal conductivity, structural flexibility and a unique porous structure, which has rapidly triggered a worldwide research boom [8–12]. In recent years, a large number of theories and experiments have shown that graphene and its derivatives can play an important role in chemical energy storage, including their use in supercapacitors, lithium-sulfur batteries, lithium-air batteries and lithium-ion batteries [13].

Graphene has amazing lithium-ion storage capacity [14–16], and many studies have reported that graphene is a potential anode material for lithium-ion batteries [17–26]. Song et al [27] used a graphene sheet prepared by oxidation and ultrasonic expansion as the anode material for lithium-ion batteries, which showed a first cycle discharge capacity of 1233 mAh/g at 0.2 mA/cm^2 and retained a discharge capacity of 502 mAh/g after 30 cycles. Wang et al. [28] showed a reversible discharge capacity of 887 mAh/g at 0.1C and maintained a discharge capacity of 730 mAh/g after 200 charge-discharge cycles. Graphene not only has excellent lithium storage performance but is also an ideal carrier for active materials. The reversible capacity and cycling stability of active materials are significantly improved when graphene is compounded with a variety of active materials that are poor in those properties, such as tin, silicon, metal oxides and metal sulfides. Graphene can synergistically enhance the electrochemical performance of active materials, mainly due to the following factors: (1) the large specific surface area of graphene can store a large amount of lithium ions, which helps to improve the specific capacity of active materials; (2) graphene has good conductivity, which is conducive to electron transport; (3) graphene has good flexibility, which is conducive to buffering the volume change of active materials caused by charging and discharging; and (4) graphene and active materials interact closely to effectively avoid aggregation between active substances.

Poizot et al. [29] was the first to report the use of transition metal (Mn, Fe, Co, Cu) oxides as anode materials for lithium-ion batteries, and a large number of transition metal oxide anode materials were studied, such as FeOx [30–33], Co_3O_4 [34–38], NiO [39–42], CuO [43–48] and ZnO [49–51]. Compared with silicon-based anode materials, transition metal oxide materials have a much smaller volume strain and higher theoretical capacity, usually in the range of 600-1000 mAh/g [52]. Assuming that their average density was 5 g/mL, their corresponding volume capacity could reach 3000-5000 mAh/g [53].

The main problems of Fe_2O_3 used as a cathode material for Li-ion batteries are as follows: (1) Fe_2O_3 has low conductivity and poor reversibility in regard to the electrode reaction, and (2) the large expansion and poor circulation of the electrode. To improve the electrochemical performance of Fe_2O_3, the following two methods can be used. The first is to make the active substances have stable micron or submicron structures. A material with this structure can provide a short lithium-ion diffusion path, which can ensure the stability of the electrode. The second is to modify the surface of the active material to reduce its loss during the electrochemical reaction. Therefore, coating the surface of an active material with a carbon material can improve the conductivity of the active material, improve the contact between the active material and electrolyte, and stabilize the electrode during cycling.

The hydrothermal method is a common preparation method. It is not only easy to perform but also easy to prepare particles with a regular morphology. Graphene has many excellent properties and unique advantages in modifying energy storage materials. The purpose of this paper is to combine the

advantages of reduced graphene oxide (RGO) with Fe_2O_3. By using cheap ferric chloride as the raw material, Fe_2O_3 and graphene are compounded by a simple hydrothermal method to prepare a graphene iron matrix composite as a new cathode material with improved electrochemical performance for use in lithium-ion batteries.

2. MATERIALS AND METHOD

All reagents were analytical grade and used without purification. XRD analysis of the material was carried out by a D/max – IIIA X-ray diffractometer. A Cu Kα radiation source was used (λ = 1.54056 Å), the test voltage was set at 30 kV, and the current was set at 30 mA. The scanning range was 10 ~ 90°, and the scanning speed was 8°/min. The decomposition process of the composites was analysed by TG-209/Vector-22 thermogravimetry infrared spectroscopy instrument in an air atmosphere. The temperature range was 20 to 900 °C, and the heating rate was 10 °C/min. The microstructure of the material was observed by transmission electron microscopy (TEM, JEM-2010HR). The acceleration voltage was 200 kV, the point resolution was 0.23 nm, and the lattice resolution was 0.14 nm. For TEM, a small amount of sample was dispersed in anhydrous ethanol, then clean filter paper was placed on a copper grid, and a clean micro-sampler was used to absorb a small amount of dispersed sample solution. The sample was added to the copper grid and dried under an infrared lamp for observation. Raman spectroscopy was carried out on a Renishaw inVia laser micro-Raman spectrometer with a 514.5 nm laser as the light source. The powdered sample could be directly pressed on a single-crystal Si wafer during sample preparation. The elemental analysis of the sample surface was carried out by X-ray photoelectron spectroscopy (XPS, Escalab 250).

A graphene oxide (GO) suspension was prepared by the Hummer's method. Briefly, 1.635 g of $FeCl_3 \cdot 6H_2O$ was added to 30 mL of water with magnetic stirring. Then, 15 mL of the GO solution was added and stirred for an additional 30 min. The mixture was transferred into a 50 mL hydrothermal pot and kept in an oven at 180 °C for 12 h. After natural cooling, the hydrothermal products were collected, filtered and washed and then dried at 80 °C for more than 12 h. Finally, the samples were collected for testing. In contrast, pure Fe_2O_3 was prepared by the same method without GO, while pure RGO was prepared directly by the hydrothermal method without the ferric chloride solution.

Electrode preparation: A certain amount of electrode active material, acetylene black and PVDF was weighed according to a mass ratio of 8:1:1. PVDF was added into an appropriate amount of NMP, stirred and dissolved for use, while the electrode active material and acetylene black were ground evenly before being added to the NMP solution with PVDF. This solution was stirred for approximately 5 h to obtain a uniform slurry. Then, the slurry was evenly coated on a dry copper foil cleaned with absolute ethanol, placed in a vacuum drying oven, and dried at 120 °C for 10 h. After cooling, the copper foil was removed, and the copper foil coated with active material was cut into electrode discs with a diameter of 14 mm. Then, the electrode disc was further pressed flat and tight by an electrode hydraulic press. The electrode was dried under an infrared lamp, and the quality of the electrode was analysed and recorded before being transferred to a glove box for assembly.

3. RESULTS AND DISCUSSION

When a GO solution is added to a ferric chloride aqueous solution, there will be slight amount of floc formation because the negatively charged GO easily combines with Fe^{3+} in the solution through electrostatic adsorption. To avoid excessive agglomeration and sedimentation, the ferric chloride solution and GO solution are mixed evenly by continuous magnetic stirring. After the solution is stirred and mixed evenly, it is poured into a hydrothermal pot for the hydrothermal reaction. During the initial stage of the reaction, the increase in temperature promotes the hydrolysis of Fe^{3+} adsorbed on GO to gradually form $Fe(OH)_3$. GO with a large number of oxygen-containing functional groups can induce the formation of particles during the initial stage. As the reaction continues, $Fe(OH)_3$ decomposes into Fe_2O_3 and is supported on GO. During the whole hydrothermal process, GO gradually removes most of the oxygen-containing groups and is finally reduced to a certain extent. In the process of Fe_2O_3 crystal growth, GO also plays a role similar to that of a surfactant. The groups on the surface of GO may selectively adsorb on some crystal faces of Fe_2O_3 crystals, resulting in a regular and uniform fusiform structure of Fe_2O_3. The formation scheme of the composite is shown in Figure 1.

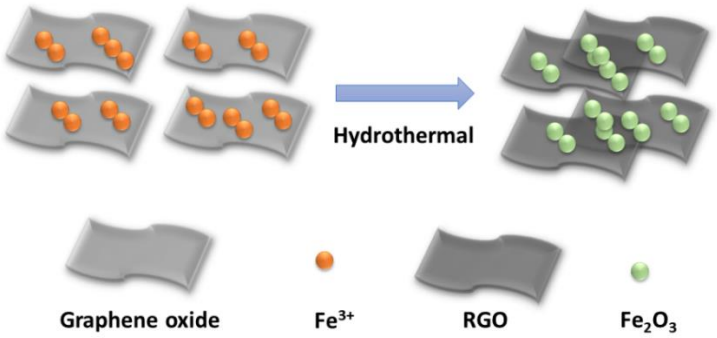

Figure 1. Hydrothermal synthesis of Fe_2O_3/RGO composites.

Figure 2 shows the TEM image of the Fe_2O_3/RGO composites. The average diameter of the Fe_2O_3 particles is calculated to be 15 nm, and they are uniformly loaded on RGO.

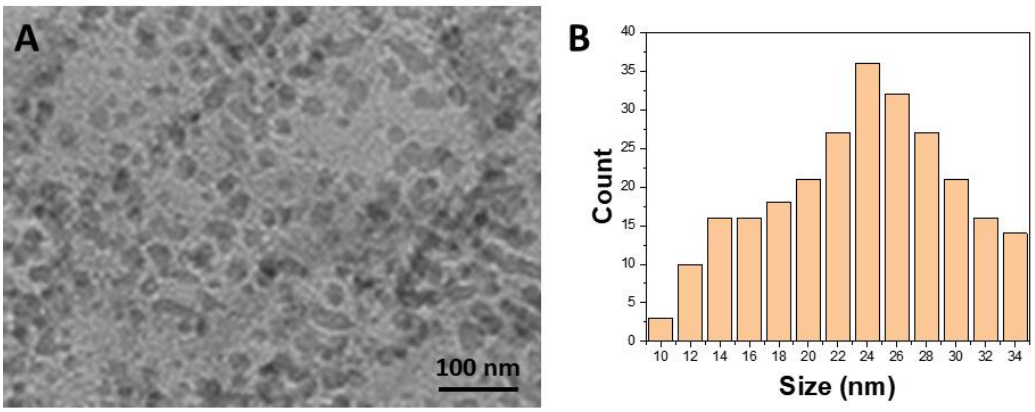

Figure 2. (A) TEM image of Fe_2O_3/RGO composite. (B) Particle size distribution of Fe_2O_3.

Figure 3A shows the XRD patterns of the Fe_2O_3, RGO and Fe_2O_3/RGO composites. It can be seen from the test results that the XRD diffraction peaks of the Fe_2O_3/RGO composite and pure Fe_2O_3 correspond to those of haematite-type Fe_2O_3 (JCPDS No. 33-0664). The diffraction peaks near 23.7°, 33.1°, 34.8°, 40.7°, 49.7°, 54.2°, 57.3°, 62.3°, 64.2°, 71.6° and 75.1° correspond to the (012), (104), (110), (113), (024), (116), (018), (214), (300), (1010) and (220) planes of haematite-type Fe_2O_3 [54,55], respectively. It is also obvious from the figure that there is a diffraction peak near 25° for both pure RGO and the Fe_2O_3/RGO composites, which corresponds to the typical diffraction peak of the (002) surface of graphite. Fe_2O_3 has no such diffraction peak, which indicates that the GO in solution is reduced after a 12 h hydrothermal reaction at 180 °C, thereby showing a certain degree of graphitization [56,57]. This result is beneficial for improving the electrical conductivity of the Fe_2O_3/RGO composite.

To determine the content of Fe_2O_3 and RGO in the Fe_2O_3/RGO composites, thermogravimetric analysis of the Fe_2O_3/RGO composites was conducted in an air atmosphere. The test results are shown in Figure 3B. It can be seen from the thermogravimetric curve that when the temperature increases to approximately 400 °C, Fe_2O_3/RGO composites begin to lose weight, corresponding to the process of RGO being oxidized to CO_2. When the temperature is increased to 550 °C, the weight loss process is complete, corresponding to the complete oxidation of all RGO, and the mass of residual material is basically unchanged. According to the calculation, the mass contents of Fe_2O_3 and RGO in the Fe_2O_3/RGO composites are approximately 80% and 20%, respectively.

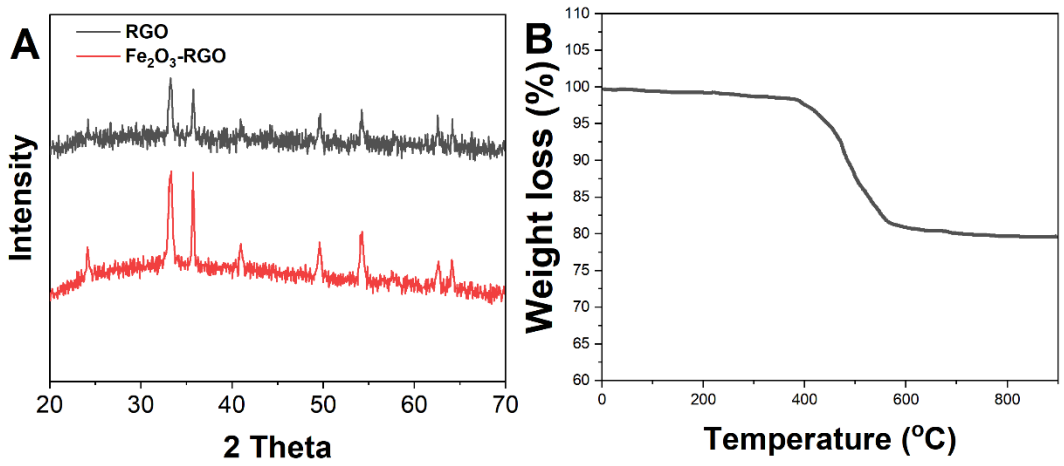

Figure 3. (A) XRD patterns of Fe_2O_3, RGO and Fe_2O_3/RGO composites. (B) TGA curve of Fe_2O_3/RGO composites.

To study the state of the elements in the Fe_2O_3/RGO composite, we performed a wide scan using XPS. As shown in the figure, the peaks observed from the Fe_2O_3/RGO composite can be assigned to C_{1s}, O_{1s}, Fe_{2p} and Fe_{3p}, indicating the existence of C, O and Fe. Figure 4B shows the narrow scan of the Fe in the Fe_2O_3/RGO composite. The results show two major peaks located at 710.9 and 724.5 eV, corresponding to $Fe_{2p3/2}$ and $Fe_{2p1/2}$, respectively, and further correspond to the Fe^{3+} in Fe_2O_3.

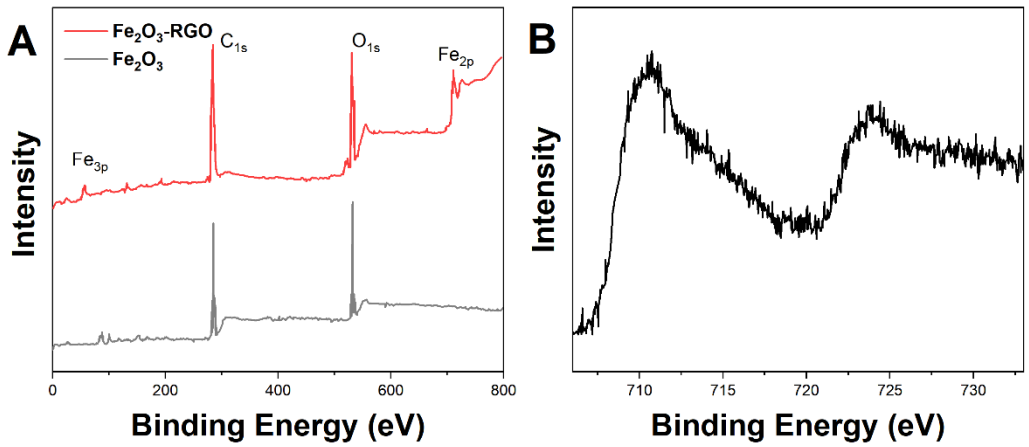

Figure 4. (A) Wide XPS spectra of Fe_2O_3/RGO composite. (B) Narrow Fe scan of Fe_2O_3/RGO composite.

Figure 5 shows the Rama spectrum of the Fe_2O_3/RGO composite. Two peaks corresponding to the D and G bands of GO are observed at 1322 and 1597 cm^{-1}. The intensity ratio of the D and G bands is 1.53, indicating the presence of defects in the composite, which can be used to improve the electro-activity. In addition, several peaks located at 218.4, 284.3, 396.5 and 596.4 cm^{-1} are observed and correspond to Ag_{1g}, E_{g2+g3}, E_{g4} and E_{g5}, respectively [58–60].

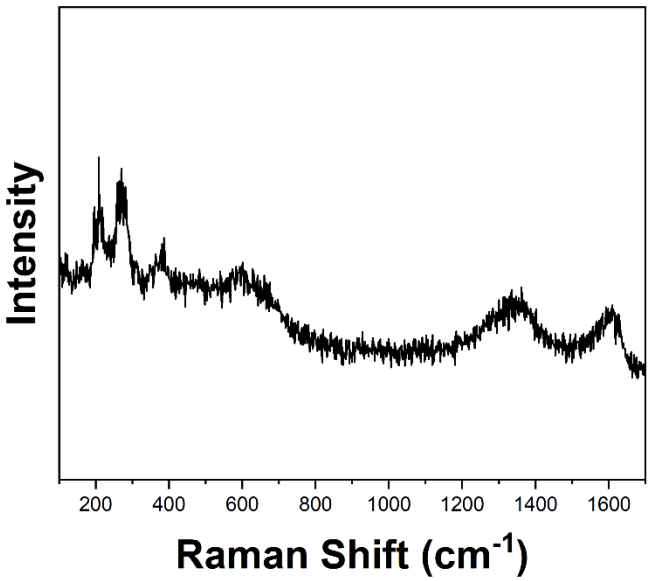

Figure 5. Raman spectrum of Fe_2O_3/RGO composite.

The electrochemical performance of the Fe_2O_3/RGO composite was tested using 2025 coin cells. Figure 6A shows the galvanostatic discharge/charge of the Fe_2O_3/RGO composite at 0.1C. Two typical plateaus are observed at 2.30 V and 2.05 V. At 0.1C, the discharge capacities of the initial cycles are

1582 mAh/g and 1503 mAh/g. Additionally, the discharge capacity remains at 812 mAh/g after 100 cycles, while the Coulombic efficiency remains 96.6% over 100 cycles.

Figure 6B shows the cycling performance of Fe_2O_3 and the Fe_2O_3/RGO composite. Fe_2O_3 without RGO shows 1285 mAh/g at the initial cycle. However, the performance decreases significantly after 100 cycles, with only 422 mAh/g remaining at the end. In contrast, the Fe_2O_3/RGO composite shows a much better performance with over 800 mAh/g remaining after 100 cycles.

The proposed Fe_2O_3/RGO composite also shows excellent performance when used at different rates. As shown in Figure 6C, the discharge capacity of the Fe_2O_3/RGO composite slowly decrease with an increasing rate. These results suggest that the Fe_2O_3/RGO composite has a stable reversible capacity at 1C. Furthermore, this result is comparable with some cathode materials, as listed in Table 1. It can be found that Fe_2O_3 has a great influence on the electrochemical properties of carbon materials. This excellent performance should be ascribed to the unique structure composed of hierarchical pores and the conductive network formed in the composite.

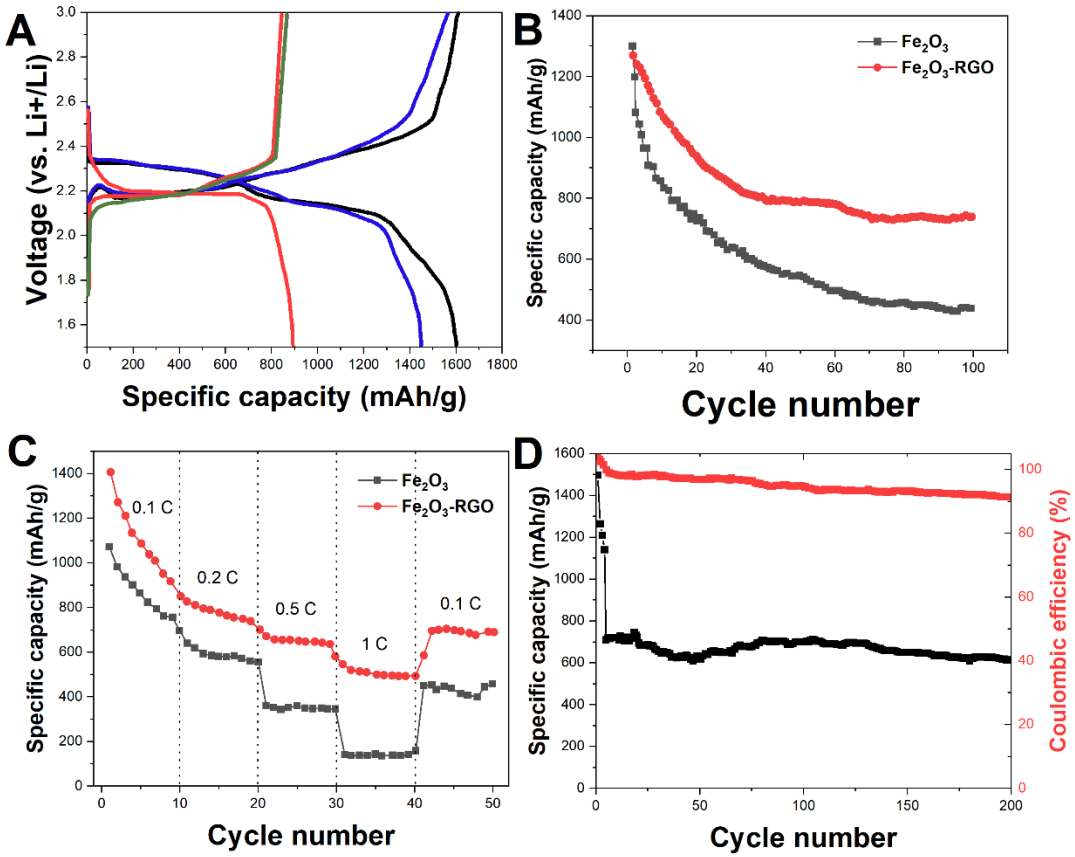

Figure 6. (A) Electrochemical performance of the Fe_2O_3/RGO composite was tested using 2025 coin cells. (B) Cycling performance of Fe_2O_3 and Fe_2O_3/RGO composite. (C) Performance of Fe_2O_3/RGO composite using different rates. (D) Long-term stability of the Fe_2O_3/RGO composite.

Figure 6D shows the long-term stability of the Fe_2O_3/RGO composite. The results show that the cathode can remain at 812 mAh/g and 633 mAh/g for over 100 cycles and 200 cycles, respectively. The Columbic efficiency can reach over 95% for each cycle. This performance may be ascribed to the large

surface area of RGO, which provides sufficient electrochemical surface area. In addition, the curl and fold of RGO can form many micropores and nano-cavities, which also shorten the diffusion path of Li ions.

Table 1. Comparison of electrochemical properties of the Fe_2O_3/RGO composite with recently literature.

Materials	Current density	Voltage range	Capacity	Reference
$Mn(VO_3)_2$@PPy	100 mA/g	1.5-4.5 V	102.6 mAh/g	[61]
KHCF@PPy	100 mA/g	2.0-4.2 V	80 mAh/g	[62]
Li_2FeSiO_4/C	100 mA/g	1.5-4.8 V	182 mAh/g	[63]
NCM811	100 mA/g	1.5-4.0 V	200 mAh/g	[64]
Fe_2O_3/RGO composite	200 mA/g	1.5-4.0 V	663 mAh/g	This work

4. CONCLUSIONS

Fe_2O_3/RGO composites were prepared via a one-pot hydrothermal synthesis by mixing ferric chloride solution and graphene oxide. This method was simple and would be easy to scale for increased production. A series of characterizations was conducted with Fe_2O_3, RGO and the Fe_2O_3/RGO composite. The Fe_2O_3 particles were small, uniform in size and uniformly loaded on RGO. The contact area between the Fe_2O_3 particles and graphene was greatly increased, which improved the conductivity of Fe_2O_3 and the cycling stability of the electrode through the conductive network formed by graphene. Compared with pure Fe_2O_3, the electrochemical performance of the Fe_2O_3/RGO composite was greatly improved.

References

1. A. Priyadharsan, V. Vasanthakumar, S. Shanavas, S. Karthikeyan, P.M. Anbarasan, *Applied Surface Science*, 470 (2019) 114–128.
2. M.A. Nasiri, P. Sangpour, S. Yousefzadeh, M. Bagheri, *Journal of Environmental Chemical Engineering*, 7 (2019) 102999.
3. Y. Yulizar, Sudirman, D.O.B. Apriandanu, J.L. Al Jabbar, *Inorganic Chemistry Communications* (2020) 108320.
4. Y. Zhu, J. Li, X. Yun, W. Zhou, L. Xi, N. Li, Z. Hu, *ACS Sustainable Chem. Eng.*, 8 (2020) 561–572.
5. L. Fu, Z. Liu, J. Ge, M. Guo, H. Zhang, F. Chen, W. Su, A. Yu, *Journal of Electroanalytical Chemistry*, 841 (2019) 142–147.
6. Z. Shamsadin-Azad, M.A. Taher, S. Cheraghi, H. Karimi-Maleh, *Journal of Food Measurement and Characterization*, 13 (2019) 1781–1787.
7. H. Karimi-Maleh, F. Karimi, S. Malekmohammadi, N. Zakariae, R. Esmaeili, S. Rostamnia, M.L. Yola, N. Atar, S. Movaghgharnezhad, S. Rajendran, A. Razmjou, Y. Orooji, S. Agarwal, V.K. Gupta, *Journal of Molecular Liquids*, 310 (2020) 113185.
8. Q. Wei, J. Sun, P. Song, J. Li, Z. Yang, Q. Wang, *Sensors and Actuators B: Chemical*, 304 (2020)

127306.
9. Y. Li, Y. Fu, S. Chen, Z. Huang, L. Wang, Y. Song, *Composites Part B: Engineering*, 171 (2019) 130–137.
10. R. Peymanfar, F. Norouzi, S. Javanshir, *Synthetic Metals*, 252 (2019) 40–49.
11. T.R. Das, P.K. Sharma, *Microchemical Journal*, 147 (2019) 1203–1214.
12. S. Frindy, M. Sillanpää, *Materials & Design*, 188 (2020) 108461.
13. F.M. Gorji, N. Monadi, *Synthetic Metals*, 258 (2019) 116199.
14. E. Yoo, J. Kim, E. Hosono, H. Zhou, T. Kudo, I. Honma, *Nano Lett.*, 8 (2008) 2277–2282.
15. G. Wang, B. Wang, X. Wang, J. Park, S. Dou, H. Ahn, K. Kim, *Journal of Materials Chemistry*, 19 (2009) 8378–8384.
16. G. Wang, X. Shen, J. Yao, J. Park, *Carbon*, 47 (2009) 2049–2053.
17. M. Mazar Atabaki, R. Kovacevic, *Electronic Materials Letters*, 9 (2013) 133–153.
18. G. Zhou, D.-W. Wang, F. Li, L. Zhang, N. Li, Z.-S. Wu, L. Wen, G.Q. (Max) Lu, H.-M. Cheng, *Chem. Mater.*, 22 (2010) 5306–5313.
19. H. Wang, L.-F. Cui, Y. Yang, H. Sanchez Casalongue, J.T. Robinson, Y. Liang, Y. Cui, H. Dai, *J. Am. Chem. Soc.*, 132 (2010) 13978–13980.
20. H. Karimi-Maleh, F. Karimi, M. Alizadeh, A.L. Sanati, *The Chemical Record*, 20 (2020) 682–692.
21. H. Karimi-Maleh, Y. Orooji, A. Ayati, S. Qanbari, B. Tanhaei, F. Karimi, M. Alizadeh, J. Rouhi, L. Fu, M. Sillanpää, *Journal of Molecular Liquids* (2020) 115062.
22. L. Fu, Y. Zheng, P. Zhang, H. Zhang, M. Wu, H. Zhang, A. Wang, W. Su, F. Chen, J. Yu, W. Cai, C.-T. Lin, *Bioelectrochemistry*, 129 (2019) 199–205.
23. J. Zhou, Y. Zheng, J. Zhang, H. Karimi-Maleh, Y. Xu, Q. Zhou, L. Fu, W. Wu, *Analytical Letters*, 53 (2020) 2517–2528.
24. L. Fu, Y. Zheng, P. Zhang, H. Zhang, Y. Xu, J. Zhou, H. Zhang, H. Karimi-Maleh, G. Lai, S. Zhao, W. Su, J. Yu, C.-T. Lin, *Biosensors and Bioelectronics*, 159 (2020) 112212.
25. Y. Xu, Y. Lu, P. Zhang, Y. Wang, Y. Zheng, L. Fu, H. Zhang, C.-T. Lin, A. Yu, *Bioelectrochemistry*, 133 (2020) 107455.
26. L. Fu, M. Wu, Y. Zheng, P. Zhang, C. Ye, H. Zhang, K. Wang, W. Su, F. Chen, J. Yu, A. Yu, W. Cai, C.-T. Lin, *Sensors and Actuators B: Chemical*, 298 (2019) 126836.
27. P. Guo, H. Song, X. Chen, *Electrochemistry Communications*, 11 (2009) 1320–1324.
28. S. Chen, P. Bao, L. Xiao, G. Wang, *Carbon*, 64 (2013) 158–169.
29. P. Poizot, S. Laruelle, S. Grugeon, L. Dupont, J. Tarascon, *Nature*, 407 (2000) 496–499.
30. H. Bian, Z. Li, J. Pan, F. Lyu, X. Xiao, J. Tang, P. Schmuki, C. Liu, J. Lu, Y.Y. Li, *Journal of Power Sources*, 484 (2021) 229268.
31. Y. Gao, Z. Shang, X. He, T. White, J. Park, X. Liang, *Electrochimica Acta*, 318 (2019) 513–524.
32. J. Li, Z. Ma, S. Hao, S. Di, L. Su, X. Qin, G. Shao, *Ionics*, 26 (2020) 2303–2314.
33. Q. Zhang, Y. Ding, A. Huang, F. Xu, X. Wang, Q. Wang, H. Lin, K. Rui, Y. Yan, Y. Shen, Y. Zhou, J. Zhu, *Chemistry – An Asian Journal*, 15 (2020) 1722–1727.
34. Y. Li, Y. Fu, W. Liu, Y. Song, L. Wang, *Journal of Alloys and Compounds*, 784 (2019) 439–446.
35. J. Wen, L. Xu, J. Wang, Y. Xiong, J. Ma, C. Jiang, L. Cao, J. Li, M. Zeng, *Journal of Power Sources*, 474 (2020) 228491.
36. M.K. Keshmarzi, A.A. Daryakenari, H. Omidvar, M. Javanbakht, Z. Ahmadi, J.-J. Delaunay, R. Badrnezhad, *Journal of Alloys and Compounds*, 805 (2019) 924–933.
37. D. Wu, C. Wang, H. Wu, S. Wang, F. Wang, Z. Chen, T. Zhao, Z. Zhang, L.Y. Zhang, C.M. Li, *Carbon*, 163 (2020) 137–144.
38. F. Zheng, L. Wei, *Journal of Alloys and Compounds*, 790 (2019) 955–962.
39. C.-F. Cheng, Y.-M. Chen, F. Zou, K. Liu, Y. Xia, Y.-F. Huang, W.-Y. Tung, M.R. Krishnan, B.D. Vogt, C.-L. Wang, R.-M. Ho, Y. Zhu, *ACS Appl. Mater. Interfaces*, 11 (2019) 30694–30702.
40. X. Yin, C. Zhi, W. Sun, L.-P. Lv, Y. Wang, *Journal of Materials Chemistry A*, 7 (2019) 7800–7814.
41. J.H. Oh, M. Su Jo, S.M. Jeong, C. Cho, Y.C. Kang, J.S. Cho, *Journal of Industrial and Engineering*

Chemistry, 77 (2019) 76–82.
42. Z. Jiang, C. Liu, L. Zhang, T. Wei, H. Jiang, J. Zhou, M. Shi, S. Liang, S. Zhang, Z. Fan, *Journal of Power Sources*, 441 (2019) 227182.
43. F. Pu, C. Kong, J. Lv, BoMa, W. Zhang, X. Zhang, S. Yang, H. Jin, Z. Yang, *Journal of Alloys and Compounds*, 805 (2019) 355–362.
44. M. Kiani, S. Omiddezyani, E. Houshfar, S.R. Miremadi, M. Ashjaee, A. Mahdavi Nejad, *Applied Thermal Engineering*, 180 (2020) 115840.
45. S. Jia, Y. Wang, X. Liu, S. Zhao, W. Zhao, Y. Huang, Z. Li, Z. Lin, *Nano Energy*, 59 (2019) 229–236.
46. H. Karimi-Maleh, O.A. Arotiba, *Journal of Colloid and Interface Science*, 560 (2020) 208–212.
47. H. Karimi-Maleh, B.G. Kumar, S. Rajendran, J. Qin, S. Vadivel, D. Durgalakshmi, F. Gracia, M. Soto-Moscoso, Y. Orooji, F. Karimi, *Journal of Molecular Liquids*, 314 (2020) 113588.
48. M. Zhang, B. Pan, Y. Wang, X. Du, L. Fu, Y. Zheng, F. Chen, W. Wu, Q. Zhou, S. Ding, *ChemistrySelect*, 5 (2020) 5035–5040.
49. G. Wu, Z. Jia, Y. Cheng, H. Zhang, X. Zhou, H. Wu, *Applied Surface Science*, 464 (2019) 472–478.
50. B. Zhao, F. Mattelaer, J. Kint, A. Werbrouck, L. Henderick, M. Minjauw, J. Dendooven, C. Detavernier, *Electrochimica Acta*, 320 (2019) 134604.
51. R. Li, W. Yue, X. Chen, *Journal of Alloys and Compounds*, 784 (2019) 800–806.
52. J.H. Moon, M.J. Oh, M.G. Nam, J.H. Lee, G.D. Min, J. Park, W.-J. Kim, P.J. Yoo, *Dalton Transactions*, 48 (2019) 11941–11950.
53. B. Banerjee, S. Lahiry, *Physica Status Solidi (a)*, 76 (1983) 683–694.
54. C. Zhang, S. Zhang, Y. Yang, H. Yu, X. Dong, *Sensors and Actuators B: Chemical*, 325 (2020) 128804.
55. K. Polat, *Solid State Communications*, 319 (2020) 113993.
56. Domga, M. Karnan, F. Oladoyinbo, G.B. Noumi, J.B. Tchatchueng, M.J. Sieliechi, M. Sathish, D.K. Pattanayak, *Electrochimica Acta*, 341 (2020) 135999.
57. J. Lyu, M. Ge, Z. Hu, C. Guo, *Chemical Engineering Journal*, 389 (2020) 124456.
58. S. A, A. Thamer, R. K, P. A, R. V, M. K, A. Murad, M. P, *Journal of Photochemistry and Photobiology B: Biology*, 207 (2020) 111885.
59. C. Song, G. Wang, F. Zhang, K. Zhu, K. Cheng, K. Ye, J. Yan, D. Cao, P. Yan, *Journal of Alloys and Compounds*, 817 (2020) 152770.
60. J. Wang, X. Yang, Y. Wang, S. Jin, W. Cai, B. Liu, C. Ma, X. Liu, W. Qiao, L. Ling, *Chemical Engineering Science* (2020) 116271.
61. H. Zhu, L. Ma, J. Jiang, Z. Xia, X. He, J. Yang, B. Yang, Q. Li, *Int. J. Electrochem. Sci*, 15 (2020) 371–381.
62. Q. Xue, L. Li, Y. Huang, R. Huang, F. Wu, R. Chen, *ACS Applied Materials & Interfaces*, 11 (2019) 22339–22345.
63. L. Qu, M. Li, P. Liu, X. Tian, Y. Yi, B. Yang, *Int. J. Electrochem. Sci*, 13 (2018) 12311–12319.
64. H. Lu, H. Zhou, A.M. Svensson, A. Fossdal, E. Sheridan, S. Lu, F. Vullum-Bruer, *Solid State Ionics*, 249 (2013) 105–111.